The dynamics of bistable liquid crystal wells

Chong Luo, Apala Majumdar, and Radek Erban
Mathematical Institute, University of Oxford, 24-29 St. Giles', Oxford, OX1 3LB, United Kingdom
e-mails: luo@maths.ox.ac.uk; majumdar@maths.ox.ac.uk; erban@maths.ox.ac.uk
(Dated: November 12, 2011)

A planar bistable liquid crystal device, reported in Tsakonas et al., is modelled within the Landau-de Gennes theory for nematic liquid crystals. This planar device consists of an array of square micron-sized wells. We obtain six different classes of equilibrium profiles and these profiles are classified as *diagonal* or *rotated* solutions. In the strong anchoring case, we propose a Dirichlet boundary condition that mimics the experimentally imposed *tangent boundary conditions*. In the weak anchoring case, we present a suitable surface energy and study the multiplicity of solutions as a function of the anchoring strength. We find that diagonal solutions exist for all values of the anchoring strength $W \geq 0$ while rotated solutions only exist for $W \geq W_c > 0$, where W_c is a critical anchoring strength that has been computed numerically. We propose a dynamic model for the switching mechanisms based on only dielectric effects. For sufficiently strong external electric fields, we numerically demonstrate diagonal to rotated and rotated to diagonal switching by allowing for variable anchoring strength across the domain boundary.

I. INTRODUCTION

Liquid crystal science has grown tremendously over the last four decades for fundamental scientific reasons and for widespread liquid crystalline applications in modern industry and technology e.g. in display devices [1], in novel functional materials and in biological sensors [2]. The simplest liquid crystal phase is the nematic phase wherein the constituent rod-like molecules have a degree of long-range orientational ordering and hence, tend to align along certain locally preferred directions [3]. The existence of such distinguished directions in nematic liquid crystals and their resulting anisotropic optical properties make nematics suitable working materials for optical devices such as displays. Recently, there has been considerable interest in the development of bistable liquid crystal displays [4, 5]. Bistable displays can support two or more stable optically contrasting liquid crystal states, so that power is only required to switch between the optically contrasting states but not to maintain a static image. Thus, bistable displays offer the promise of a new generation of larger, economical and high-resolution displays that are very lucrative for industry.

Bistable displays typically use a combination of complex surface morphologies and surface treatments to stabilize multiple liquid crystal states [4–6]. Examples of bistable displays include the two-dimensional Zenithally Bistable Nematic (ZBD) device [6] and the three-dimensional Post Aligned Bistable Nematic (PABN) device [5]. The ZBD device consists of a liquid crystal layer sandwiched between two solid surfaces where the bottom surface is featured by a complex wedge-shaped grating. Both surfaces are treated to induce *homeotropic* (*normal*) boundary conditions and the ZBD cell supports two static stable states: the defect-free Vertically Aligned Nematic (VAN) state and the Hybrid Aligned Nematic (HAN) state which is distinguished by defects near the wedge-shaped grating [6]. The PABN cell has a three-dimensional structure with a liquid crystal layer sandwiched between two solid substrates and the bottom substrate is featured by an array of microscopic posts. Unlike the ZBD cell, the boundary conditions for the PABN cell are of a mixed type. The top substrate is treated to induce homeotropic boundary conditions whilst the bottom substrate and the post surfaces are treated to have *tangent* (*planar*) boundary conditions. Experimental observations and optical modelling suggest that there are at least two competing static stable states: the opaque *tilted* state and the transparent *planar* state [5].

In this paper, we focus on the two-dimensional bistable liquid crystal device investigated both experimentally and numerically by Tsakonas et al. [7]. This device consists of an array of square wells filled with nematic liquid crystal material. The well surfaces are treated to induce *tangent boundary conditions* i.e. the liquid crystal molecules in contact with the well surfaces are constrained to be in the plane of the surfaces. When viewed between crossed polarizers, the authors observe two classes of stable equilibria in this geometry: *diagonal* states where the liquid crystal molecules align along the square diagonals and *rotated* states where the direction of alignment rotates by π across the width of the cell. The experimental results are also accompanied by modelling in the Landau-de Gennes framework [7].

We build on the results in [7] within the Landau-de Gennes framework [3] and model the device on a two-dimensional square or rectangular domain. This is equivalent to neglecting structural variations across the height of the cell and focussing on the structural variations across the square cross-section. We first formulate the modelling problem in terms of a Dirichlet boundary-value problem and introduce the concept of an *optimal* Dirichlet boundary condition. There are multiple choices of Dirichlet boundary conditions consistent with the experimentally imposed tangent

boundary conditions and we formulate the *optimal* Dirichlet boundary condition as the solution of a variational problem. We then consider the more physically realistic weak anchoring situation where we relax the Dirichlet boundary condition and impose an appropriate surface energy characterized by an anchoring strength W. The resulting mathematical problem is well-posed, yields physically realistic equilibria for all values of the anchoring strength $W > 0$ and the weak anchoring equilibria converge to the strong anchoring equilibria in the limit of infinite anchoring. We numerically compute bifurcation diagrams for the equilibria in the weak anchoring case and study the multiplicity of stable equilibria as a function of the anchoring strength. We numerically find six different classes of solutions, two of which are labelled as *diagonal* and four of which are labelled as *rotated* based on their alignment structures. The diagonal solutions exist for all $W \geq 0$, whereas the rotated solutions only exist for anchoring strengths above a certain critical value $W_c > 0$. We estimate this critical anchoring strength in terms of the material parameters and find that the system is bistable/multistable for $W \geq W_c$.

We propose a simple dynamic model based on the gradient flow approach for the switching characteristics of this device. This model only relies on dielectric effects and we do not need to incorporate flexoelectricity unlike other models in the existing literature [8]. Our dynamic model does not account for viscous dissipation or fluid-flow effects but simply gives a qualitative description of the mechanisms that drive the switching procedure. To achieve switching from diagonal to rotated and vice-versa, we make the anchoring strength on one of the square edges much weaker than that on the remaining three square edges and we apply a uniform electric field along the square diagonals.

The paper is organized as follows. In section II, we review the Landau-de Gennes $\boldsymbol{Q}$-tensor theory for liquid crystals. In section III, we study the strong anchoring problem. In section IV, we study the weak anchoring problem and present bifurcation diagrams for the corresponding equilibria as a function of the anchoring strength. In section V, we demonstrate a switching mechanism between the competing stable states under the action of an external electric field. Finally, in Appendix, we elaborate on the numerical methods.

II. TWO-DIMENSIONAL (2D) LANDAU-DE GENNES THEORY

The Oseen-Frank theory is the simplest continuum theory for nematic liquid crystals, based on the assumption of strict uniaxiality (a single distinguished direction of molecular alignment) and a constant degree of orientational ordering [9]. In the Oseen-Frank framework, the liquid crystal configuration is modelled by a unit-vector field $\boldsymbol{n}$ (often referred to as *director* because of the $\boldsymbol{n} \to -\boldsymbol{n}$ symmetry), which represents the locally preferred direction of molecular alignment. The Oseen-Frank theory assigns a free energy to every admissible $\boldsymbol{n}$ and working in the simplest one-constant approximation, the Oseen-Frank energy reduces to the well-known Dirichlet energy below [10]

$$\mathcal{E}_{OF}[\boldsymbol{n}] := \int_{\Omega} \frac{1}{2} K |\nabla \boldsymbol{n}|^2 \, \mathrm{d}A, \tag{1}$$

where $\Omega \subset \mathbb{R}^2$ is the physical domain, $\mathrm{d}A$ is the corresponding area element and $K > 0$ is an elastic constant. To have finite Oseen-Frank energy (1), the admissible $\boldsymbol{n}$ must belong to the Sobolev space $H^1(\Omega, S^1)$, the space of unit-vector fields with square-integrable first derivatives [11].

However, the Oseen-Frank theory is not well-suited to model the planar square (or rectangular) bistable device reported in Tsakonas et al. [7]. As stated in the previous section, the tangent boundary conditions constrain the liquid crystal molecules in contact with the well surfaces to be in the plane of the well surfaces [12]. Taking the modelling domain to be a square or a rectangle and working in the Oseen-Frank framework, this implies that the unit-vector field $\boldsymbol{n}$ is constrained to be tangent to the square/rectangle edges i.e. $\boldsymbol{n}$ is aligned horizontally on the horizontal edges and vertically on the vertical edges. Thus, $\boldsymbol{n}$ is necessarily discontinuous at the vertices where two or more edges meet. However, it has been shown in [13] that unit-vector fields with jump discontinuous Dirichlet boundary condition do not belong to $H^1(\Omega)$ for $\Omega \in \mathbb{R}^2$, and hence have infinite Oseen-Frank energy (1). This difficulty can be resolved by introducing an order parameter that can vanish at defect locations i.e. we need to relax the assumption of constant orientational ordering in the Oseen-Frank framework.

We model the planar bistable device by a rectangular domain

$$\Omega = \left\{ (x, y) \in \mathbb{R}^2 : x \in [0, L] \,, \; y \in [0, a_r \times L] \right\}, \tag{2}$$

where L is the width of the rectangle and a_r is the aspect ratio. We work within the Landau-de Gennes framework [3, 14, 15], whereby the liquid crystal configuration is modelled by a symmetric traceless tensor $\boldsymbol{Q}$. In the 2D case, the $\boldsymbol{Q}$-tensor can be written as

$$\boldsymbol{Q} = s(2\boldsymbol{n} \otimes \boldsymbol{n} - I), \tag{3}$$

where $\boldsymbol{n} = \boldsymbol{n}(x, y)$ is an eigenvector, $s = s(x, y)$ is a scalar order parameter that measures the degree of orientational ordering about $\boldsymbol{n}$ and I is the 2×2 identity matrix [10]. Unlike the Oseen-Frank theory, the order parameter s in the $\boldsymbol{Q}$-tensor model varies across the modelling domain and in particular, vanishes at the vertices as required.

The $\boldsymbol{Q}$-tensor is invariant under the transformation $\boldsymbol{n} \to -\boldsymbol{n}$ and preserves the head-to-tail symmetry of the nematic molecules [16]. Since $\boldsymbol{Q}$ is symmetric and traceless, we can write it in the following matrix form

$$\boldsymbol{Q} = \begin{pmatrix} Q_{11} & Q_{12} \\ Q_{12} & -Q_{11} \end{pmatrix}. \tag{4}$$

Any 2D unit-vector field $\boldsymbol{n}$ can be written in terms of an angle θ in the (x, y)-plane as shown below

$$\boldsymbol{n}(x, y) = (\cos\theta(x, y), \sin\theta(x, y)). \tag{5}$$

Then one can readily check that

$$Q_{11} = s\cos(2\theta), \tag{6}$$
$$Q_{12} = s\sin(2\theta). \tag{7}$$

Also, we have

$$\mathrm{tr}(\boldsymbol{Q}) = \mathrm{tr}(\boldsymbol{Q}^3) = 0, \tag{8}$$
$$\mathrm{tr}\boldsymbol{Q}^2 = 2s^2. \tag{9}$$

In the absence of external fields and surface effects, the Landau-de Gennes energy functional is given by

$$\mathcal{E}_{LDG} = \mathcal{E}_{el} + \mathcal{E}_B, \tag{10}$$

where $\mathcal{E}_{el}$ is an elastic energy and $\mathcal{E}_B$ is the bulk energy [15, 16]. In the simplest case, the elastic energy is given by

$$\mathcal{E}_{el}[\boldsymbol{Q}] := \int_\Omega \frac{L_{el}}{2} |\nabla \boldsymbol{Q}|^2 \, \mathrm{d}A, \tag{11}$$

where $L_{el} > 0$ is an elastic constant [3, 16]. The bulk energy is given by

$$\mathcal{E}_B[\boldsymbol{Q}] := \int_\Omega \overline{\alpha}(T)\mathrm{tr}\boldsymbol{Q}^2 - \frac{b^2}{3}\mathrm{tr}\boldsymbol{Q}^3 + \frac{c^2}{4}(\mathrm{tr}\boldsymbol{Q}^2)^2 \, \mathrm{d}A, \tag{12}$$

where $\overline{\alpha}(T) = \gamma(T - T^*)$ with $\gamma > 0$, T denotes the absolute temperature and T^* is a characteristic temperature below which the disordered isotropic phase loses its stability [16]. Further, b^2 and c^2 are positive material-dependent constants [3, 15]. We work in the low-temperature regime and in this case, for a fixed temperature $T < T^*$, we can write the bulk energy as -

$$\mathcal{E}_B[\boldsymbol{Q}] = \int_\Omega -\frac{\alpha^2}{2}\mathrm{tr}\boldsymbol{Q}^2 - \frac{b^2}{3}\mathrm{tr}\boldsymbol{Q}^3 + \frac{c^2}{4}(\mathrm{tr}\boldsymbol{Q}^2)^2 \, \mathrm{d}A, \tag{13}$$

where $\alpha^2 > 0$ is a temperature-dependent and material-dependent constant. In 2D, one can directly verify that

$$\mathcal{E}_{el}[\boldsymbol{Q}] = \int_\Omega L_{el} \left(|\nabla Q_{11}|^2 + |\nabla Q_{12}|^2 \right) \, \mathrm{d}A, \tag{14}$$

and

$$\mathcal{E}_B[\boldsymbol{Q}] = \int_\Omega c^2 s^4 - \alpha^2 s^2 \, \mathrm{d}A. \tag{15}$$

The bulk energy $\mathcal{E}_B$ achieves its minimum at

$$s \equiv s_0 = \sqrt{\frac{\alpha^2}{2c^2}}. \tag{16}$$

We define

$$\varepsilon^2 := \frac{1}{c^2}, \tag{17}$$

then $\mathcal{E}_B$ can be rewritten as

$$\mathcal{E}_B[\boldsymbol{Q}] = \int_\Omega \frac{1}{\varepsilon^2}(s^2 - s_0^2)^2 - \frac{s_0^4}{\varepsilon^2}\,\mathrm{d}A. \tag{18}$$

Therefore up to an additive constant, the Landau-de Gennes energy is given by

$$\mathcal{E}_{LDG}[\boldsymbol{Q}] = \int_\Omega L_{el}\left(|\nabla Q_{11}|^2 + |\nabla Q_{12}|^2\right) + \frac{1}{\varepsilon^2}(Q_{11}^2 + Q_{12}^2 - s_0^2)^2\,\mathrm{d}A. \tag{19}$$

In the strong anchoring case, the eigenvector $\boldsymbol{n}$ in (3) is constrained to be strictly tangent to the edges of the rectangular domain i.e. $\boldsymbol{n} = \pm\mathbf{e}_x$ on the horizontal edges and $\boldsymbol{n} = \pm\mathbf{e}_y$ on the vertical edges where $\mathbf{e}_x$ and $\mathbf{e}_y$ are the unit-vectors in the x and y-coordinate directions respectively. These boundary conditions are encoded by a Dirichlet boundary condition $(Q_{11}, Q_{12}) = \boldsymbol{g}$, for some Lipschitz continuous $\boldsymbol{g}$ and we will prescribe an appropriate form of $\boldsymbol{g}$ in the next section.

In the weak anchoring case, the Dirichlet boundary condition $(Q_{11}, Q_{12}) = \boldsymbol{g}$ is replaced by a surface anchoring energy which favours the tangent boundary conditions. We have studied three different candidates for the surface anchoring energy. The first choice is given by

$$\mathcal{E}_A[\boldsymbol{Q}] := \int_{\partial\Omega} \frac{W\boldsymbol{\nu}\cdot\boldsymbol{Q}\boldsymbol{\nu}}{\sqrt{Q_{11}^2 + Q_{12}^2}}\,\mathrm{d}a, \tag{20}$$

where $\mathrm{d}a$ is the line element on $\partial\Omega$, $\boldsymbol{\nu}$ is the outward unit-normal vector on $\partial\Omega$, and $W = W(x, y)$ is the anchoring strength on $\partial\Omega$ which might take different values across the boundary. We assume W is a constant in most part of this paper, unless otherwise specified. The energy (20) is equivalent to the widely-used Rapini-Papoular surface energy

$$\int_{\partial\Omega} 2W\sin^2(\theta - \theta_0)\,\mathrm{d}a, \tag{21}$$

where θ_0 denotes the preferred orientation on the boundary [17]. However, this surface energy has the following shortcomings (i) the energy density is discontinuous at $(Q_{11}, Q_{12}) = (0, 0)$ and (ii) for large $W > 0$, we are numerically unable to compute the corresponding equilibria because of convergence problems. A second choice for the surface anchoring energy is

$$\mathcal{E}_A[\boldsymbol{Q}] := \int_{\partial\Omega} W\boldsymbol{\nu}\cdot\boldsymbol{Q}\boldsymbol{\nu}\,\mathrm{d}a, \tag{22}$$

as has been used in [7]. For a fixed $\varepsilon > 0$, the order parameter s becomes unbounded in the limit $W \to \infty$, leading to non-physical solutions. The third and the most suitable choice is the following surface anchoring energy proposed in [16]

$$\mathcal{E}_A[\boldsymbol{Q}] := \int_{\partial\Omega} W\left|(Q_{11}, Q_{12}) - \boldsymbol{g}\right|^2\,\mathrm{d}a, \tag{23}$$

where $\boldsymbol{g}$ is the Dirichlet boundary condition for the strong anchoring problem. For a suitable choice of $\boldsymbol{g}$, this surface energy enjoys the following advantages as will be demonstrated in the subsequent numerical results: (i) we can find equilibrium solutions for arbitrarily large $W > 0$, (ii) the order parameters s are bounded in the limit $W \to \infty$ and (iii) as $W \to \infty$, the weak anchoring solutions converge to the corresponding strong anchoring solutions in $H^1(\Omega, \mathbb{R}^2)$. The properties of the three different surface anchoring energies (20), (22) and (23) are summarized in Table I.

Model	Existence for large W	Boundedness of s	Convergence to strong anchoring
(20)	✗	✓	✗
(22)	✓	✗	✗
(23)	✓	✓	✓

TABLE I: *Comparison of the different surface energies* (20), (22) *and* (23).

To model the switching dynamics of this bistable device, an external electric field must be included into the formulation. In the Landau-de Gennes framework, the electrostatic energy is given by

$$\mathcal{E}_E[\boldsymbol{Q}] := \int_\Omega -\frac{1}{2}\epsilon_0(\boldsymbol{\epsilon}\boldsymbol{E})\cdot\boldsymbol{E} - \boldsymbol{P}_s\cdot\boldsymbol{E}\,\mathrm{d}A, \tag{24}$$

where $\boldsymbol{E}$ is the electric field vector, $\boldsymbol{P}_s$ is the spontaneous polarization vector, $\boldsymbol{\epsilon}$ is the dielectric tensor and can be approximated by $\boldsymbol{\epsilon} = \triangle\epsilon^*\boldsymbol{Q} + \bar{\epsilon}I$, and ϵ_0, $\triangle\epsilon^*$, and $\bar{\epsilon}$ are material-dependent constants [16]. In particular, $\triangle\epsilon^*$ is the dielectric anisotropy and we work with materials that have positive dielectric anisotropy in what follows. For symmetric rod-like liquid crystal molecules, we can neglect flexoelectricity (or P_s) and the electrostatic energy then simplifies to

$$\mathcal{E}_E[\boldsymbol{Q}] = \int_\Omega -C_0(\boldsymbol{Q}\boldsymbol{E})\cdot\boldsymbol{E}\,\mathrm{d}A, \tag{25}$$

with $C_0 = \frac{1}{2}\epsilon_0\triangle\epsilon^*$. Let $\boldsymbol{E} = |\boldsymbol{E}|(\cos\theta_E, \sin\theta_E)$ for some angle θ_E. Substituting into (25), we find that

$$\mathcal{E}_E[\boldsymbol{Q}] = \int_\Omega -C_0|\boldsymbol{E}|^2(Q_{11}\cos(2\theta_E) + Q_{12}\sin(2\theta_E))\,\mathrm{d}A. \tag{26}$$

The total energy is the sum of the elastic energy $\mathcal{E}_{el}$, the bulk energy $\mathcal{E}_B$, the surface anchoring energy $\mathcal{E}_A$ and the electrostatic energy $\mathcal{E}_E$ as shown below -

$$\begin{aligned}\mathcal{E}[\boldsymbol{Q}] = &\int_\Omega L_{el}\left(|\nabla Q_{11}|^2 + |\nabla Q_{12}|^2\right) + \frac{1}{\varepsilon^2}(Q_{11}^2 + Q_{12}^2 - s_0^2)^2\,\mathrm{d}A\\ &+ \int_{\partial\Omega} W\left|(Q_{11}, Q_{12}) - \boldsymbol{g}\right|^2\,\mathrm{d}a\\ &+ \int_\Omega -C_0|\boldsymbol{E}|^2(Q_{11}\cos(2\theta_E) + Q_{12}\sin(2\theta_E))\,\mathrm{d}A.\end{aligned} \tag{27}$$

Before we proceed with the analysis and numerical computations, we non-dimensionalize the system as follows. Take the reference domain to be $\tilde{\Omega} = [0,1]\times[0,a_r]$ and let $\tilde{x} = x/L$, $\tilde{y} = y/L$. Define new variables

$$(\tilde{Q}_{11}, \tilde{Q}_{12}) := (Q_{11}, Q_{12})/s_0, \tag{28}$$

$$\tilde{\boldsymbol{g}} := \boldsymbol{g}/s_0, \tag{29}$$

and

$$\tilde{\varepsilon} := \frac{\varepsilon\sqrt{L_{el}}}{L}, \tag{30}$$

$$\tilde{W} := \frac{WL}{L_{el}}, \tag{31}$$

$$\tilde{E} := \frac{L|\boldsymbol{E}|}{s_0}\sqrt{\frac{|C_0|}{L_{el}}}. \tag{32}$$

Then the total energy $\mathcal{E}$ can be written in terms of these dimensionless variables -

$$\begin{aligned}\frac{1}{s_0^2 L_{el}}\mathcal{E}[\boldsymbol{Q}] = &\int_{\tilde{\Omega}}\left(|\nabla\tilde{Q}_{11}|^2 + |\nabla\tilde{Q}_{12}|^2\right) + \frac{1}{\tilde{\varepsilon}^2}(\tilde{Q}_{11}^2 + \tilde{Q}_{12}^2 - 1)^2\,\mathrm{d}\tilde{A}\\ &+ \int_{\partial\tilde{\Omega}}\tilde{W}\left|(\tilde{Q}_{11}, \tilde{Q}_{12}) - \tilde{\boldsymbol{g}}\right|^2\,\mathrm{d}\tilde{a}\\ &+ \int_{\tilde{\Omega}} -\mathrm{sgn}(C_0)\tilde{E}^2(\tilde{Q}_{11}\cos(2\theta_E) + \tilde{Q}_{12}\sin(2\theta_E))\,\mathrm{d}\tilde{A},\end{aligned} \tag{33}$$

where $\mathrm{d}\tilde{A}$ and $\mathrm{d}\tilde{a}$ are the area element in $\tilde{\Omega}$ and the line element on $\partial\tilde{\Omega}$ respectively. In what follows, we work with the dimensionless energy $\tilde{\mathcal{E}} := \mathcal{E}/(s_0^2 L_{el})$.

Some typical values of the physical parameters are $1/\varepsilon^2 = 1\times10^6\,\mathrm{N\,m^{-1}}$, $L_{el} = 10^{-11}\,\mathrm{Nm}$, $s_0 = 0.6$, $L = 8\times10^{-5}\,\mathrm{m}$ and $W = 2\times10^{-3}\mathrm{N}$, as given in [7]. By (30), the dimensionless parameter $\tilde{\varepsilon}$ is about 6.6×10^{-5}. Since $\tilde{\varepsilon}$ is so small, we can view the bulk energy density $\frac{1}{\tilde{\varepsilon}^2}(\tilde{Q}_{11}^2 + \tilde{Q}_{12}^2 - 1)^2$ as a penalty term that enforces $\tilde{Q}_{11}^2 + \tilde{Q}_{12}^2 = 1$ a.e. in $\tilde{\Omega}$. For simplicity, we remove the tilde's in the following sections and all the variables and parameters are dimensionless unless otherwise specified.

III. STRONG ANCHORING

In the strong anchoring case, the dimensionless energy functional is

$$\mathcal{E}[\boldsymbol{Q}] = \int_\Omega \left(|\nabla Q_{11}|^2 + |\nabla Q_{12}|^2\right) + \frac{1}{\varepsilon^2}(Q_{11}^2 + Q_{12}^2 - 1)^2 \,\mathrm{d}A \tag{34}$$

accompanied by a Dirichlet boundary condition $(Q_{11}, Q_{12}) = \boldsymbol{g}$. We note that (34) is precisely the Ginzburg-Landau energy functional for superconductors, which has been extensively studied in the literature [10, 18].

The boundary condition $\boldsymbol{g}$ has to be carefully chosen as we now describe. In the strong in-plane anchoring situation, the eigenvector $\boldsymbol{n}$ in (3) is constrained to be strictly tangent to the boundary. On the top and bottom edges, $\theta = 0$ or π and hence by (6) and (7) we have

$$Q_{11} = s, \tag{35}$$
$$Q_{12} = 0, \tag{36}$$

where $s^2 = Q_{11}^2 + Q_{12}^2$. On the left and right edges, $\theta = \pi/2$ or $-\pi/2$ and thus

$$Q_{11} = -s, \tag{37}$$
$$Q_{12} = 0. \tag{38}$$

We take s to be strictly non-negative on the boundary. Therefore, solutions of the strong anchoring problem satisfy the following conditions:

$$Q_{11} \geq 0 \text{ on horizontal edges,} \tag{39}$$
$$Q_{11} \leq 0 \text{ on vertical edges and,} \tag{40}$$
$$Q_{12} = 0 \text{ on } \partial\Omega. \tag{41}$$

Any Lipschitz continuous function $\boldsymbol{g} : \partial\Omega \to \mathbb{R}^2$ that satisfies the conditions (39)-(41) results in a well-posed energy minimization problem. For any Lipschitz continuous $\boldsymbol{g}$, the admissible space

$$\mathcal{A}_{\boldsymbol{g}} = \{\boldsymbol{u} \in H^1(\Omega, \mathbb{R}^2) : \boldsymbol{u} = \boldsymbol{g} \text{ on } \partial\Omega\} \tag{42}$$

is non-empty [19]. Furthermore, since the energy functional (34) is coercive and convex in ∇Q, we are guaranteed the existence of a global energy minimizer in $\mathcal{A}_{\boldsymbol{g}}$ [20].

For any fixed Dirichlet boundary condition $\boldsymbol{g}$, we can use standard tools in the calculus of variations to show that local minimizers (Q_{11}, Q_{12}) of the energy functional (34) in the admissible set $\mathcal{A}_{\boldsymbol{g}}$ are solutions of the following integral equations -

$$0 = \int_\Omega \nabla Q_{11} \nabla v_{11} + \frac{2}{\varepsilon^2}\left(Q_{11}^2 + Q_{12}^2 - 1\right) Q_{11} v_{11} \,\mathrm{d}A \qquad \forall v_{11} \in H_0^1(\Omega) \tag{43}$$

$$0 = \int_\Omega \nabla Q_{12} \nabla v_{12} + \frac{2}{\varepsilon^2}\left(Q_{11}^2 + Q_{12}^2 - 1\right) Q_{12} v_{12} \,\mathrm{d}A \qquad \forall v_{12} \in H_0^1(\Omega). \tag{44}$$

We discretize the system and solve it using finite element methods [21]. The details of the numerical methods can be found in Appendix.

We find that for each fixed Lipschitz continuous $\boldsymbol{g}$, there are typically six distinct equilibrium solutions. We categorize these six solutions as either *diagonal* or *rotated*, according to their director profiles. There are two diagonal solutions, which we label as D1 and D2 respectively, and four rotated solutions, which we label as R1, R2, R3 and R4 respectively. The director profiles of these six solutions are shown in Figure 1. We find that amongst the six solutions, the two diagonal solutions are energetically degenerate whilst the four rotated solutions are energetically degenerate. However, the rotated solutions have slightly higher energies than those of the corresponding diagonal solutions.

In what follows, we choose an appropriate Lipschitz continuous $\boldsymbol{g}$ as the fixed boundary condition for the Dirichlet problem to be studied in this paper. For each fixed ε, a different choice of the Dirichlet boundary condition $\boldsymbol{g}$ yields a different set of diagonal and rotated solutions. There is an optimal Dirichlet boundary condition $\boldsymbol{g}_{D1}$ whose D1-diagonal solution has the minimum energy in the space of all D1-type diagonal solutions. Similarly, there is an optimal Dirichlet boundary condition for each of the other five solution types too. Let (Q_{11}, Q_{12}) be a local minimizer of (34) in the admissible space

$$\mathcal{A} = \{(u_1, u_2) \in H^1(\Omega, \mathbb{R}^2) : u_2 = 0 \text{ on } \partial\Omega\}. \tag{45}$$

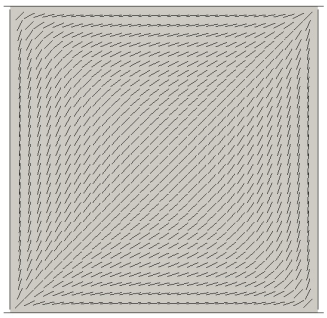

(a)D1

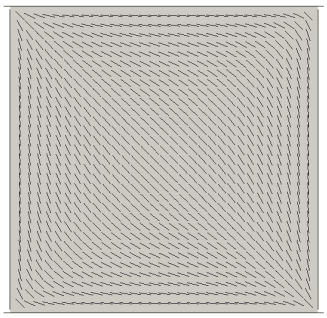

(b)D2

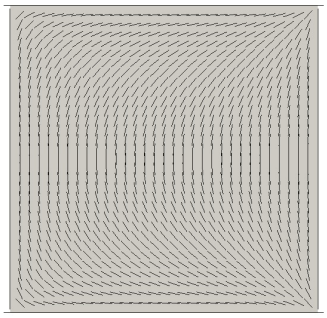

(c)R1

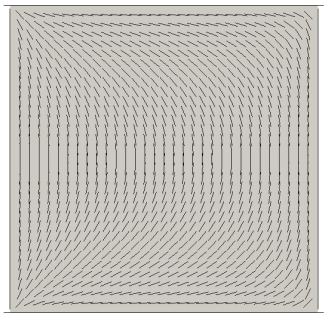

(d)R2

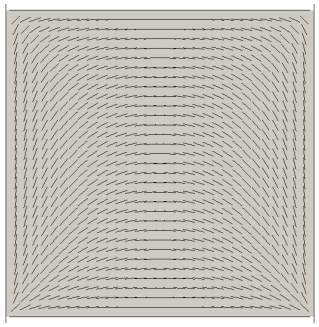

(e)R3

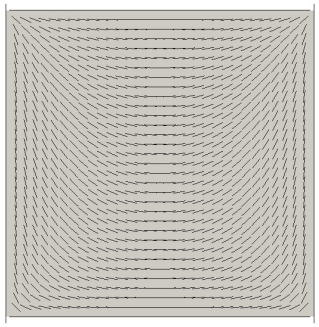

(f)R4

FIG. 1: *The six types of solutions of (43) –(44).*

Then (Q_{11}, Q_{12}) satisfies the following integral equations

$$0 = \int_\Omega \nabla Q_{11} \nabla v_{11} + \frac{2}{\varepsilon^2}\left(Q_{11}^2 + Q_{12}^2 - 1\right) Q_{11} v_{11} \, \mathrm{d}A \qquad \forall v_{11} \in H^1(\Omega) \tag{46}$$

$$0 = \int_\Omega \nabla Q_{12} \nabla v_{12} + \frac{2}{\varepsilon^2}\left(Q_{11}^2 + Q_{12}^2 - 1\right) Q_{12} v_{12} \, \mathrm{d}A \qquad \forall v_{12} \in H_0^1(\Omega). \tag{47}$$

Solutions of (46)-(47) are defined to be *optimal solutions*, and the corresponding traces on $\partial\Omega$ are labelled as *optimal boundary conditions*. Although the optimal solutions are computed with the constraint (41), numerical results show that the optimal diagonal and rotated solutions satisfy the constraints (39) and (40) too.

In Figure 2, we plot the scaled order parameter s for the optimal D1 and R2-solutions. The *scaled order parameter* s is defined to be $s := \sqrt{Q_{11}^2 + Q_{12}^2}$, where the scaled parameters Q_{11} and Q_{12} are given by (28) (with tildes removed). We can see that s achieves its minimum at the four corners, and this minimum is zero for the diagonal D1-solution and non-zero (about 0.02) for the rotated R2-solution.

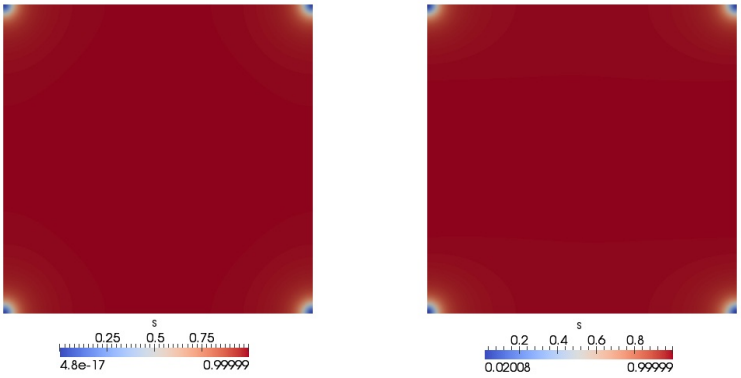

(a)The order parameter of the optimal D1-solution.

(b)The order parameter of the optimal R2-solution.

FIG. 2: *(Color online) Plot of the scaled order parameter s for the optimal solutions. Parameters:* $\varepsilon = 0.02$*, mesh size* $N = 128$ *and* $a_r = 1$.

We comment briefly on the notion of an optimal boundary condition. For small ε, the optimal boundary conditions enforce $s = 1$ almost everywhere on the square/rectangle boundary except for at the vertices where $s = 0$. The optimal boundary condition prescribes the optimal interpolation between $s = 0$ to $s = 1$ on the edges i.e. the interpolation with the minimum associated energy cost. The optimal boundary conditions depend on ε and numerical results show that for each $\varepsilon > 0$, there are six optimal Dirichlet boundary conditions : $\boldsymbol{g}_{D1}, \boldsymbol{g}_{D2}, \boldsymbol{g}_{R1}, \boldsymbol{g}_{R2}, \boldsymbol{g}_{R3}, \boldsymbol{g}_{R4}$ with $\boldsymbol{g}_{D1} = \boldsymbol{g}_{D2}$, $\boldsymbol{g}_{R1} = \boldsymbol{g}_{R2}$, and $\boldsymbol{g}_{R3} = \boldsymbol{g}_{R4}$. However, $\boldsymbol{g}_{D1} \neq \boldsymbol{g}_{R1} \neq \boldsymbol{g}_{R3}$. On the one hand, we find that $\boldsymbol{g}_{D1}$ is very close to the average $(\boldsymbol{g}_{R1} + \boldsymbol{g}_{R3})/2$ and their maximum difference is proportional to ε^4, as shown in Figure 3. On the other hand, the maximum differences $|\boldsymbol{g}_{D1} - \boldsymbol{g}_{R1}|$ and $|\boldsymbol{g}_{R1} - \boldsymbol{g}_{R3}|$ are proportional to ε^2, as shown in Figure 4. Therefore, the differences between the optimal boundary conditions tend to zero as ε tends to zero.

In the following sections, we fix the Dirichlet boundary condition to be $\boldsymbol{g} = \boldsymbol{g}_{D1}$, which is the optimal boundary condition for the D1-solutions, and use this to define an appropriate surface energy in the next section.

IV. WEAK ANCHORING

In this section, we study the weak anchoring situation and replace the Dirichlet boundary condition with the surface anchoring energy (23). The total dimensionless energy is given by

$$\begin{aligned}\mathcal{E}[\boldsymbol{Q}] = &\int_\Omega |\nabla Q_{11}|^2 + |\nabla Q_{12}|^2 + \frac{1}{\varepsilon^2}(Q_{11}^2 + Q_{12}^2 - 1)^2 \, \mathrm{d}A \\ &+ \int_{\partial\Omega} W \left|(Q_{11}, Q_{12}) - \boldsymbol{g}\right|^2 \, \mathrm{d}a,\end{aligned} \tag{48}$$

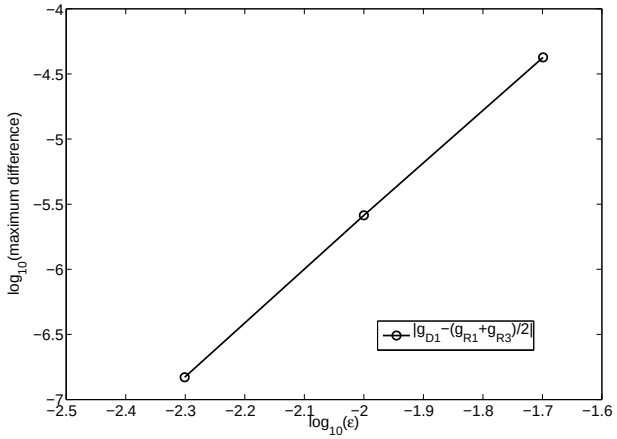

FIG. 3: *Plot of* $Y := \log_{10} |\boldsymbol{g}_{D1} - (\boldsymbol{g}_{R1} + \boldsymbol{g}_{R3})/2|$ *versus* $X := log_{10}\varepsilon$. *The fitted equation is* $Y = 2.56 + 4.08X$. *Parameters: mesh size* $N = 256$ *and* $a_r = 1$.

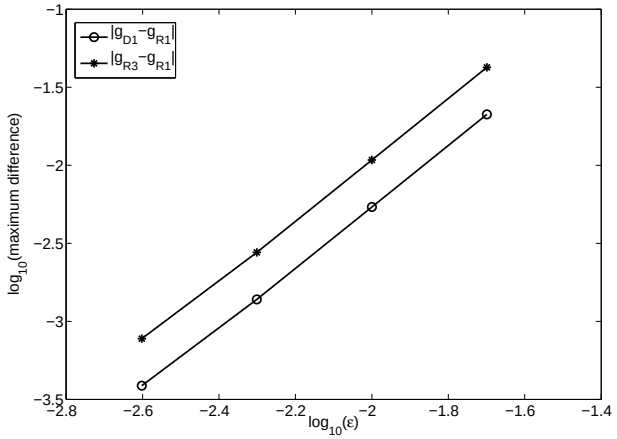

FIG. 4: *Plot of* $Y_1 := \log_{10} |\boldsymbol{g}_{D1} - \boldsymbol{g}_{R1}|$ *and* $Y_2 := \log_{10} |\boldsymbol{g}_{R3} - \boldsymbol{g}_{R1}|$ *versus* $X := \log_{10} \varepsilon$. *The fitted equations are* $Y_1 = 1.59 + 1.93X$ *and* $Y_2 = 1.90 + 1.93X$. *Parameters: mesh size* $N = 256$ *and* $a_r = 1$.

where $\boldsymbol{g} = \boldsymbol{g}_{D1}$ is the Dirichlet boundary condition for the strong anchoring problem studied in Section III. This Dirichlet boundary condition depends on the choice of ε as explained in the previous section. The admissible space for (Q_{11}, Q_{12}) is simply the Sobolev space $H^1(\Omega, \mathbb{R}^2)$.

By calculus of variations, local energy minimizers of (48) satisfy the following integral equations

$$\begin{aligned} 0 = &\int_\Omega \nabla Q_{11} \nabla v_{11} + \frac{2}{\varepsilon^2} \left(Q_{11}^2 + Q_{12}^2 - 1\right) Q_{11} v_{11} \, \mathrm{d}A \\ &+ \int_{\partial\Omega} W(Q_{11} - g_1) v_{11} \, \mathrm{d}a \qquad \forall v_{11} \in H^1(\Omega) \end{aligned} \tag{49}$$

$$\begin{aligned} 0 = &\int_\Omega \nabla Q_{12} \nabla v_{12} + \frac{2}{\varepsilon^2} \left(Q_{11}^2 + Q_{12}^2 - 1\right) Q_{12} v_{12} \, \mathrm{d}A \\ &+ \int_{\partial\Omega} W(Q_{12} - g_2) v_{12} \, \mathrm{d}a \qquad \forall v_{12} \in H^1(\Omega), \end{aligned} \tag{50}$$

where $(g_1, g_2) = \boldsymbol{g}$. Again we discretize these equations and solve using finite element methods; the details can be found in Appendix.

Figure 5 shows the scaled order parameter s for the D1-diagonal weak anchoring solution. We can see that s achieves its minimum at the four corners. Unlike the strong anchoring case, the minimal s is non-zero (about 0.3). It is noteworthy that the scaled order parameters of the weak anchoring solutions are bounded for all $W > 0$.

For a fixed anchoring strength $W > 0$, there exist multiple weak anchoring solutions. To see how these solutions vary with the anchoring strength, we trace the solution branches using pseudo arc-length continuation [22]. The

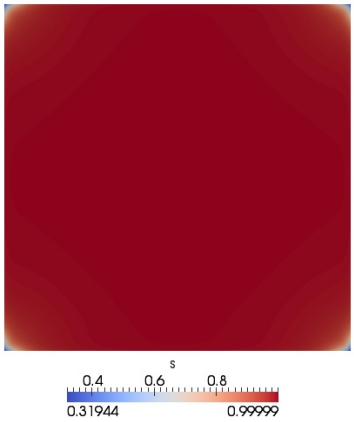

FIG. 5: *(Color online) Plot of the scaled order parameter s for the* D1*-weak anchoring solution. Parameters:* $\varepsilon = 0.02$*,* $W = 50$*, mesh size* $N = 128$ *and* $a_r = 1$*.*

resulting bifurcation diagram for $\varepsilon = 0.02$ and $a_r = 1$ is shown in Figure 6, where the x-axis is the anchoring strength W and the y-axis is the average of the angles over half of the top edge $\{(x, 1) : 0 < x < \frac{1}{2}\}$ (with unit π). We find that this average is suitable for distinguishing between the different solution profiles and is a better measure than the average over the whole top edge. For example, in the case of the R3 and R4-solutions, the directors at the top edge are symmetric about the mid-point of the top edge and thus the average over the entire top edge is around $\pi/2$ in both cases. By plotting typical director profiles from each solution branch, we find that for large enough $W > 0$, the six solutions from top to bottom are R4, D2, R2, R1, D1, and R3 respectively (see Figure 1 to recall the corresponding director profiles). We note that the diagonal solutions, D1 and D2, exist for all $W \geq 0$ while the rotated solutions, R1, R2, R3 and R4, only exist for $W \geq W_c \approx 2.7$. Further, the R1 and R2-solutions are in the same branch while the R3 and R4-solutions are in the same branch. We find that at $W = 0$, the D1-solutions degenerate to the constant solution $(Q_{11}, Q_{12}) \equiv (0, 1)$ (which corresponds to $\theta \equiv \pi/4$), while the D2-solutions degenerate to the constant solution $(Q_{11}, Q_{12}) \equiv (0, -1)$ (which corresponds to $\theta \equiv 3\pi/4$). At $W = W_c$, although the director profiles show that R1 and R2-solutions degenerate to a solution with $\theta \equiv \pi/2$ and the R3 and R4-solutions degenerate to a solution with $\theta \equiv 0$, these degenerate solutions do not have constant (Q_{11}, Q_{12}) values across the domain. Since $\boldsymbol{g}$ is not constant on $\partial\Omega$, constant solutions cannot satisfy the equations (49)-(50) at $W = W_c > 0$. We have produced videos that demonstrate how the solutions change as we move along the bifurcation diagram and these videos can be found at Supplemental Online Information (which is temporarily located at `http://www.maths.ox.ac.uk/~luo/bswitch.html`).

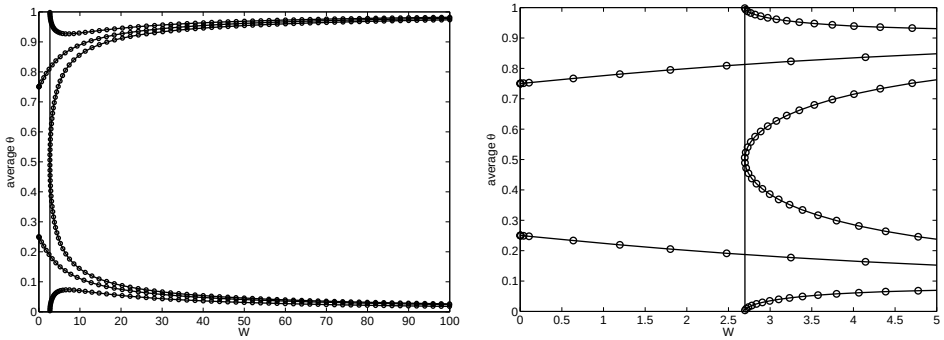

(a)The whole picture.

(b)Zoom-in near the critical anchoring strength.

FIG. 6: *The bifurcation diagram. Parameters:* $\varepsilon = 0.02$*, mesh size* $N = 32$ *and* $a_r = 1$*.*

We have studied the stability of the distinct equilibria and have found that all six equilibria in Figure 6 are stable. The details of the stability analysis can be found in Appendix. As $W \to \infty$, the weak anchoring solutions converge to their strong anchoring counterparts in $H^1(\Omega)$, as shown in Figure 7. This is a pre-requisite for any viable surface anchoring energy.

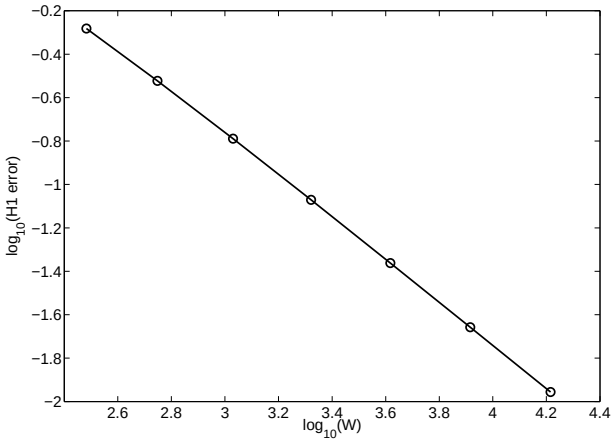

FIG. 7: *Plot of* $Y := \log_{10} \|\boldsymbol{u}_W - \boldsymbol{u}\|_1$ *versus* $X := \log_{10} W$*, where* $\boldsymbol{u}_W$ *is the weak anchoring* D1*-solution at anchoring strength* W *and* $\boldsymbol{u}$ *is the strong anchoring* D1*-solution (see section III). The fitted equation is* $Y = 2.14 - 0.97X$*. Parameters:* $\varepsilon = 0.02$*, mesh size* $N = 32$ *and* $a_r = 1$*.*

Figure 8 illustrates how the critical anchoring strength W_c varies with the parameter ε. Recall that ε is related to the material parameters by (30). We can see that W_c decreases linearly as $\varepsilon \to 0$. The fitted equation is $W_c(\varepsilon) = 2.54 + 10.30\varepsilon$, which suggests that W_c might remain a positive constant in the limit $\varepsilon \to 0$. That is, in the limit $\varepsilon \to 0$, the rotated solutions do not exist unless the anchoring strength is sufficiently strong. This is consistent with the global energy-minimizing property of the diagonal solutions.

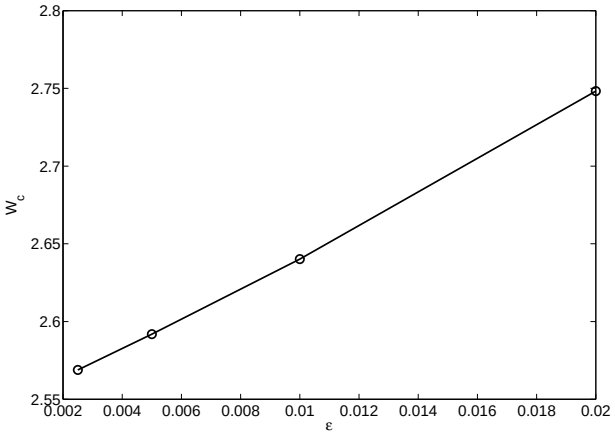

FIG. 8: *Critical anchoring strength* W_c *versus* ε*. The fitted equation is* $W_c(\varepsilon) = 2.54 + 10.30\varepsilon$*. Parameters: mesh size* $N = 256$ *and* $a_r = 1$*.*

V. SWITCHING UNDER ELECTRIC FIELD

In this section, we model the switching mechanisms between different stable states under the action of an external electric field, in the weak anchoring set-up.

By gradient flow analysis, the dynamic equations associated with the dimensionless free energy in (33) are given by

[20]

$$\begin{aligned}\frac{\partial Q_{11}}{\partial t} =&\triangle Q_{11} - \frac{2}{\varepsilon^2}\left(Q_{11}^2 + Q_{12}^2 - 1\right) Q_{11} \\ &- \frac{1}{2}\mathrm{sgn}(C_0)E^2\cos(2\theta_E) \quad \text{in } \Omega,\end{aligned} \tag{51}$$

$$\begin{aligned}\frac{\partial Q_{12}}{\partial t} =&\triangle Q_{12} - \frac{2}{\varepsilon^2}\left(Q_{11}^2 + Q_{12}^2 - 1\right) Q_{12} \\ &- \frac{1}{2}\mathrm{sgn}(C_0)E^2\sin(2\theta_E) \quad \text{in } \Omega,\end{aligned} \tag{52}$$

$$\frac{\partial Q_{11}}{\partial t} = -\frac{\partial Q_{11}}{\partial \boldsymbol{\nu}} - W(Q_{11} - g_1) \quad \text{on } \partial\Omega, \tag{53}$$

$$\frac{\partial Q_{12}}{\partial t} = -\frac{\partial Q_{12}}{\partial \boldsymbol{\nu}} - W(Q_{12} - g_2) \quad \text{on } \partial\Omega, \tag{54}$$

where $(g_1, g_2) = \boldsymbol{g}_{D1}$, as stated in section IV. Here t is dimensionless and can be related to the physical time $\tilde{t}$ by

$$t = \frac{L_{el}}{\gamma L^2}\tilde{t}, \tag{55}$$

and γ is a viscosity coefficient with units $\mathrm{N\,s\,m^{-1}}$ [23]. We use the finite difference method [24] to simulate the dynamics under electric field. We discretize the rectangular domain using uniform $N \times (N \cdot a_r)$ mesh, approximate the Laplace operator $\triangle$ using five-point stencil, approximate $\partial/\partial\boldsymbol{\nu}$ using backward difference and approximate $\partial/\partial t$ using forward difference [24].

A typical switching process consists of two steps. In the first step, we switch on the electric field and wait for the system to reach equilibrium. In the second step, we switch off the electric field and wait for the system to reach equilibrium again. In the following numerical simulation, the system is regarded to be in the equilibrium state when the l^2-difference [25] between adjacent states is less than $\tau = 10^{-3}$.

We first investigate the situation of constant anchoring strength W on $\partial\Omega$. We find that the rotated to diagonal switching can be easily achieved by applying uniform electric fields in the diagonal directions. The diagonal to rotated switching is more difficult to accomplish. We have achieved switching from D1 to R2-solutions using the following patched electric fields on a square domain

$$\boldsymbol{E} = \begin{cases} 10(\cos(\pi/4), \sin(\pi/4)) & y \in [0, 1/8) \\ 10(\cos(\pi/2), \sin(\pi/2)) & y \in [1/8, 7/8] \\ 10(\cos(3\pi/4), \sin(3\pi/4)) & y \in (7/8, 1] \end{cases}$$

and by using the following linear electric fields on a rectangular domain with $a_r = 2$

$$\boldsymbol{E} = 10\frac{y}{a_r}(\cos(3\pi/4), \sin(3\pi/4)). \tag{56}$$

However, these non-uniform electric fields are not easy to implement in practice because the physical domain can be as small as 80μm [7].

Using a non-uniform anchoring strength on the boundary can also facilitate diagonal to rotated switching and this can be much easier to physically implement than non-uniform electric fields. One possible framework is to make the anchoring strength on the top edge much weaker than that on the rest of the domain boundary. For example,

$$W = \begin{cases} 10 & \text{on } y = a_r, \\ 100 & \text{otherwise.} \end{cases} \tag{57}$$

With the anchoring strength given by (57), the R2 to D1 switching can be achieved using

$$\boldsymbol{E} = 10(\cos(\pi/4), \sin(\pi/4)),$$

and the D1 to R2 switching can be achieved using

$$\boldsymbol{E} = 10(\cos(3\pi/4), \sin(3\pi/4)). \tag{58}$$

We can qualitatively understand this switching phenomenon by recalling the D1 and R2-alignment profiles from Figure 1. The D1-solutions correspond to the boundary conditions, $\theta(x,0) = \theta(x,a_r) = 0$ and $\theta(0,y) = \theta(1,y) = \frac{\pi}{2}$, whereas the R2-solutions correspond to the boundary conditions, $\theta(x,0) = 0, \theta(x,a_r) = \pi, \theta(0,y) = \theta(1,y) = \frac{\pi}{2}$. Hence, the two solution profiles are distinguished by their alignment profile on the top edge. In (57), we have made the anchoring strength on the top edge ten times smaller than that on the remaining three edges so that the non-equilibrium configurations in the presence of the uniform diagonal electric field (58) can break the anchoring on the top edge and then relax into the R2-state once the electric field is removed.

Figure 9 demonstrates the switching mechanism from R2 to D1 while Figure 10 shows the switching mechanism from D1 to R2. Note that for the same electric field strength, the switching from D1 to R2 is slightly slower than the switching from R2 to D1. This is possibly because the D1-solution has lower energy than the R2-solution and there is a higher energy barrier to be overcome before the system can get out of the D1-equilibrium.

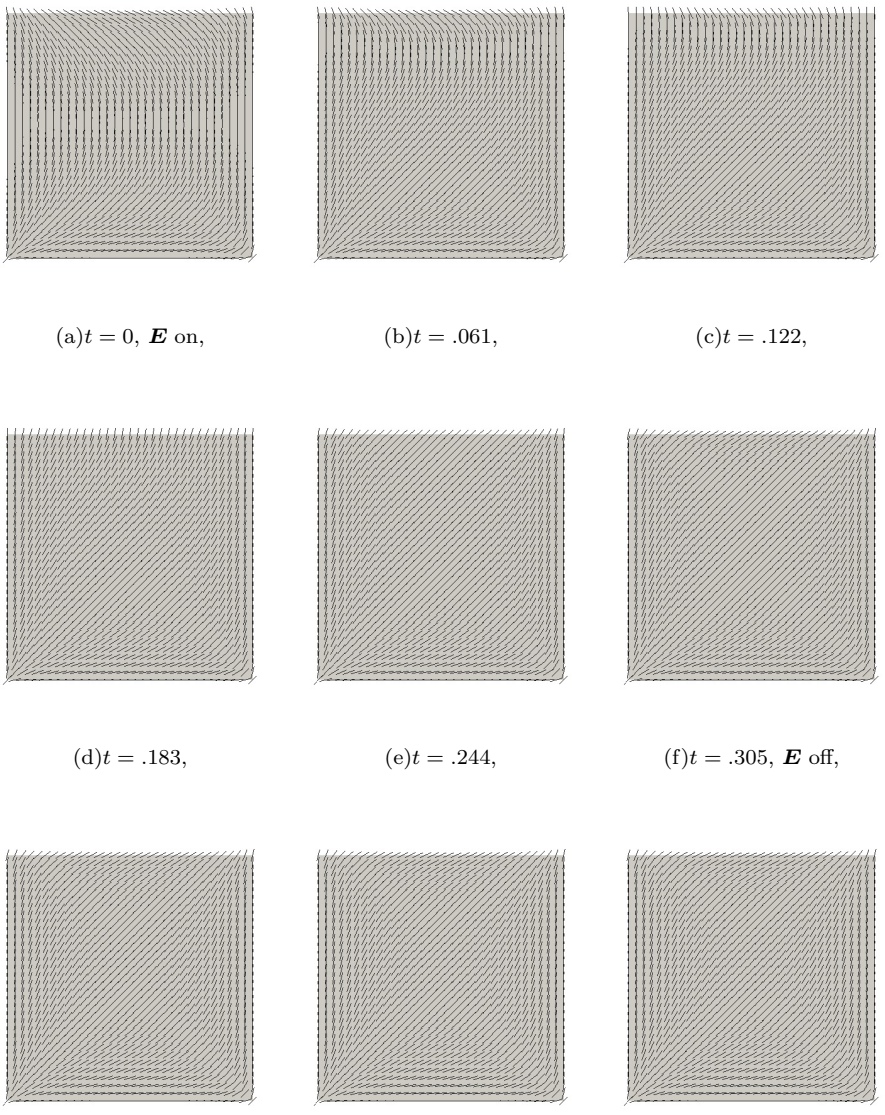

(a)$t = 0$, $\boldsymbol{E}$ on, (b)$t = .061$, (c)$t = .122$,

(d)$t = .183$, (e)$t = .244$, (f)$t = .305$, $\boldsymbol{E}$ off,

(g)$t = .320$, (h)$t = .336$, (i)$t = .351$.

FIG. 9: *The switching from* R2 *to* D1. *Parameters:* $\varepsilon = 0.02$, $\boldsymbol{E} = 10(\cos(\pi/4), \sin(\pi/4))$, *mesh size* $N = 32$, *time-step* $\triangle t = 1/N^3$, $\tau = 10^{-3}$, *and* W *is given by* (57).

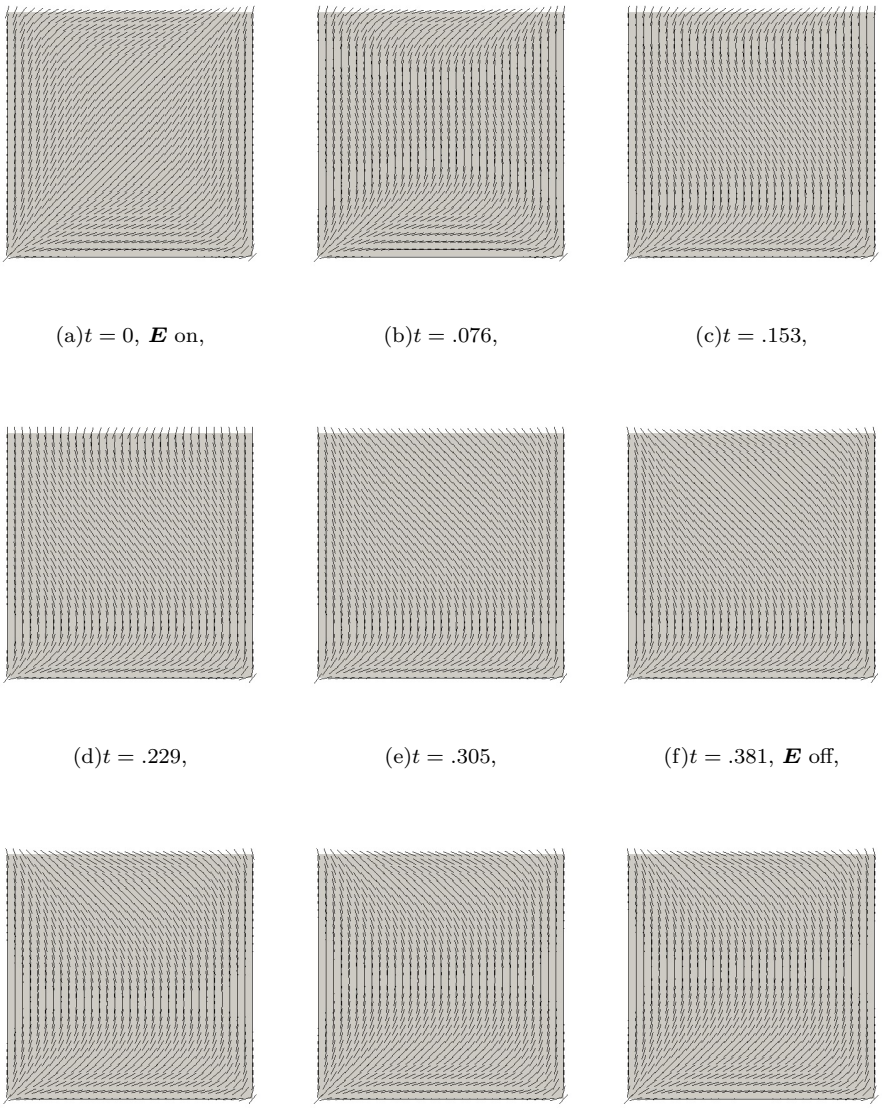

(a)$t = 0$, $\boldsymbol{E}$ on, (b)$t = .076$, (c)$t = .153$,

(d)$t = .229$, (e)$t = .305$, (f)$t = .381$, $\boldsymbol{E}$ off,

(g)$t = .430$, (h)$t = .479$, (i)$t = .528$.

FIG. 10: *The switching from* D1 *to* R2. *Parameters:* $\varepsilon = 0.02$, $\boldsymbol{E} = 10(\cos(3\pi/4), \sin(3\pi/4))$, *mesh size* $N = 32$, *time-step* $\triangle t = 1/N^3$, $\tau = 10^{-3}$, *and* W *is given by* (57).

VI. CONCLUSIONS

We have mathematically modelled and analysed a planar bistable liquid crystal device with tangent boundary conditions, as has been reported in [7]. We have modelled the static equilibria and the switching mechanisms in this device within the Landau-de Gennes theory for nematic liquid crystals. We have introduced the concept of an optimal Dirichlet boundary condition which, in turn, depends on the material parameters ε, L_{el} and the device width L through the dimensionless parameter $\tilde{\varepsilon}$. In the weak anchoring case, we have proposed a surface anchoring energy in terms of an anchoring coefficient W and the optimal Dirichlet boundary condition i.e. the surface anchoring energy incorporates coupling effects between the surface anchoring strength W and bulk parameters such as ε and L_{el}. We have studied the multiplicity and the stability of static equilibria as a function of the anchoring strength W and have found that the device is bistable/multistable for $W \geq W_c > 0$, where the critical anchoring strength W_c depends on

material parameters through the dimensionless variable $\tilde{\varepsilon}$. For $W \geq W_c$, we have found six competing static equilibria which mimic the experimentally observed diagonal and rotated profiles in [7]. We have investigated the dependence of W_c on the parameter $\tilde{\varepsilon}$ and numerical investigations indicate a linear scaling.

We proposed a simple dynamic model for the switching characteristics of this device that is based on dielectric effects and the concept of variable anchoring strength across the domain boundary. The anchoring is weaker on the subset of the boundary which induces the transition between two stable static equilibria. We have studied the switching between the D1- and R2-solutions and the same concepts can be applied to study switching between different pairs of static equilibria.

Appendix: Numerical Methods

In this section, we give some technical details for the numerical methods. We have solved the integral equations (43)–(44), (46)–(47) and (49)–(50) with finite element methods. Recall that (43)-(44) correspond to the strong anchoring solutions, (46)–(47) correspond to the optimal solutions and (49)–(50) correspond to the weak anchoring solutions. We partition the domain $\Omega = [0,1] \times [0, a_r]$ into a uniform $N \times (a_r \cdot N)$ triangular mesh and approximate $H^1(\Omega)$ using piecewise linear finite elements [21]. After the discretization, the integral equations become a nonlinear system of equations for the degrees of freedom, (Q_{11}, Q_{12}), and are solved using Newton's method [24]. Newton's method strongly depends on the initial condition and to obtain the six different solutions D1∼R4, we simply use six different initial conditions.

For a given Dirichlet boundary condition $\boldsymbol{g}$, we construct the initial conditions for the strong anchoring problem as follows. Take the D1-solution for example. We first solve the Laplace equation $\triangle\theta = 0$ on the uniform mesh using finite difference method with the discontinuous boundary condition: $\theta(0,y) = \theta(1,y) = \frac{\pi}{2}$ and $\theta(x,0) = \theta(x,a_r) = 0$. Next we construct $(Q_{11}, Q_{12}) = s(\cos 2\theta, \sin 2\theta)$, where $s = 1$ at the interior nodes and $s = |\boldsymbol{g}|$ at the boundary nodes. Then we use the resulting (Q_{11}, Q_{12}) as the initial condition for the strong anchoring D1-solution. In Table II, we enumerate the boundary conditions for all six types of initial conditions. For a fixed $d > 0$, we define the vector field

solution	$x = 0$	$x = 1$	$y = 0$	$y = a_r$
D1	$\pi/2$	$\pi/2$	0	0
D2	$\pi/2$	$\pi/2$	π	π
R1	$\pi/2$	$\pi/2$	π	0
R2	$\pi/2$	$\pi/2$	0	π
R3	$3\pi/2$	$\pi/2$	π	π
R4	$\pi/2$	$3\pi/2$	π	π

TABLE II: *The six different initial conditions for Newton's method.*

$\boldsymbol{g}_d$ to be

$$\boldsymbol{g}_d = \begin{cases} (T_d(x), 0) & \text{on } y = 0 \text{ and } y = a_r, \\ \left(-T_{\frac{d}{a_r}}\left(\frac{y}{a_r}\right), 0\right) & \text{on } x = 0 \text{ and } x = 1, \end{cases} \tag{A.1}$$

where the trapezoidal shape function $T_d : [0,1] \to \mathbb{R}$ is given by

$$T_d(t) = \begin{cases} t/d & 0 \leq t \leq d, \\ 1 & d \leq t \leq 1-d, \\ (1-t)/d & 1-d \leq t \leq 1. \end{cases} \tag{A.2}$$

The parameter d is in the range $d \in (0, 0.5]$. To obtain the optimal solutions, we use the strong anchoring solutions for $\boldsymbol{g} = \boldsymbol{g}_{3\varepsilon}$ as the initial conditions. For the weak anchoring solutions with large anchoring strength $W > 0$, we use the strong anchoring solutions as initial conditions for Newton's method. Then we use numerical continuation to obtain solutions for smaller W.

Once we obtain the solutions with Newton's method, we compute their energies by numerical integration techniques. In this paper, all finite element simulations and numerical integrations have been performed using the open-source package FEniCS [26].

Tables III, IV and V show the numerical errors, energies and their orders of convergence for some typical optimal solutions, strong anchoring solutions and weak anchoring solutions respectively. We can see that in all cases, we have

order 2 convergence for the L^2-errors and the total energies, and order 1 convergence for the H^1-errors. We also observe that in all cases the diagonal solutions have lower energies than the rotated solutions.

The optimal D1 solution						
N	L^2 err	order	H^1 err	order	Energy	order
16	3.71E-02		2.80E+00		90.803	
32	1.15E-02	1.68	1.65E+00	0.76	81.337	1.74
64	3.31E-03	1.80	8.74E-01	0.92	78.500	1.89
128	8.76E-04	1.92	4.43E-01	0.98	77.734	1.96
256	2.23E-04	1.97	2.22E-01	0.99	77.538	1.99
The optimal R2 solution						
N	L^2 err	order	H^1 err	order	Energy	order
16	3.99E-02		2.85E+00		99.878	
32	1.19E-02	1.74	1.67E+00	0.77	90.056	1.76
64	3.39E-03	1.81	8.82E-01	0.92	87.153	1.89
128	8.93E-04	1.92	4.47E-01	0.98	86.373	1.97
256	2.27E-04	1.98	2.24E-01	0.99	86.173	1.99

TABLE III: *Numerical errors, energies and their orders of convergence for the optimal solutions. Parameters:* $\varepsilon = 0.02$ *and* $a_r = 1$.

The rotated solution R2						
N	L^2 err	order	H^1 err	order	Energy	order
16	4.04E-02		2.85E+00		99.896	
32	1.19E-02	1.77	1.67E+00	0.77	90.056	1.76
64	3.38E-03	1.81	8.82E-01	0.92	87.155	1.89
128	8.90E-04	1.92	4.47E-01	0.98	86.375	1.97
256	2.26E-04	1.98	2.24E-01	0.99	86.175	1.99
The rotated solution R3						
N	L^2 err	order	H^1 err	order	Energy	order
16	4.04E-02		2.85E+00		99.896	
32	1.19E-02	1.77	1.67E+00	0.77	90.056	1.76
64	3.38E-03	1.81	8.82E-01	0.92	87.155	1.89
128	8.90E-04	1.92	4.47E-01	0.98	86.375	1.97
256	2.26E-04	1.98	2.24E-01	0.99	86.175	1.99

TABLE IV: *Numerical errors, energies and their orders of convergence for the strong anchoring solutions. Parameters:* $\varepsilon = 0.02$ *and* $a_r = 1$.

Next, we give details for the stability analysis in the weak anchoring case. By gradient flow analysis [20], solutions of the weak anchoring problem satisfy the following dynamic equations

$$\frac{\partial Q_{11}}{\partial t} = \triangle Q_{11} - \frac{2}{\varepsilon^2}\left(Q_{11}^2 + Q_{12}^2 - 1\right) Q_{11} \quad \text{in } \Omega, \tag{A.3}$$

$$\frac{\partial Q_{12}}{\partial t} = \triangle Q_{12} - \frac{2}{\varepsilon^2}\left(Q_{11}^2 + Q_{12}^2 - 1\right) Q_{12} \quad \text{in } \Omega, \tag{A.4}$$

$$\frac{\partial Q_{11}}{\partial t} = -\frac{\partial Q_{11}}{\partial \boldsymbol{\nu}} - W(Q_{11} - g_1) \quad \text{on } \partial\Omega, \tag{A.5}$$

$$\frac{\partial Q_{12}}{\partial t} = -\frac{\partial Q_{12}}{\partial \boldsymbol{\nu}} - W(Q_{12} - g_2) \quad \text{on } \partial\Omega. \tag{A.6}$$

We first apply finite difference discretization [24] to the dynamic equations (A.3)-(A.6), approximating $\frac{\partial}{\partial t}$ using forward difference, $\frac{\partial}{\partial \boldsymbol{\nu}}$ using backward difference, and the Laplacian $\triangle$ using five-point stencil on a uniform $N \times (a_r \cdot N)$ mesh. We denote the mesh width as $h = 1/N$ and the time-step size as $\triangle t$. After discretization, the dynamic equations can

The diagonal solution D1						
N	L^2 err	order	H^1 err	order	Energy	order
32	6.63E-03		1.08E+00		64.448	
64	1.81E-03	1.88	5.81E-01	0.90	62.928	1.98
128	4.64E-04	1.96	2.96E-01	0.97	62.544	1.99
256	1.17E-04	1.98	1.49E-01	0.99	62.446	1.99
The rotated solution R2						
N	L^2 err	order	H^1 err	order	Energy	order
32	7.25E-03		1.11E+00		73.156	
64	1.93E-03	1.91	5.91E-01	0.90	71.579	1.99
128	4.95E-04	1.97	3.02E-01	0.97	71.181	1.99
256	1.25E-04	1.99	1.52E-01	0.99	71.081	1.99

TABLE V: *Numerical errors, energies and their orders of convergence for the weak anchoring solutions. Parameters:* $\varepsilon = 0.02$, $W = 50$ *and* $a_r = 1$.

be written as a discrete map $\boldsymbol{u}^{(n+1)} = f(\boldsymbol{u}^{(n)})$, where $\boldsymbol{u}^{(n)}$ is the solution at time-step n. The linear stability of an equilibrium solution $\boldsymbol{u}$ is then determined by $f'(\boldsymbol{u})$ [27]. It is easy to check that $f'(\boldsymbol{u}) = I - \gamma A$, where $\gamma = \triangle t/h^2$ and $A = A(\boldsymbol{u})$ is a non-symmetric matrix . In the limit $\triangle t \to 0$, the asymptotic linear stability of an equilibrium solution $\boldsymbol{u}$ is then simply determined by the positivity of the smallest eigenvalue λ_1 of the matrix A. It turns out $A = DB$, where D is a diagonal matrix and B is a symmetric matrix. The diagonal entries of D are either 1 or h, with the former corresponding to interior nodes and the latter corresponding to edge nodes. The smallest eigenvalue of A is then computed by applying the ARPACK++ package [28] to the symmetric matrix $D^{1/2}BD^{1/2}$, which can be verified to have the same spectrum as the matrix $A = DB$.

Acknowledgments

We thank Prof. Nigel Mottram for helpful discussion. This publication was based on work supported in part by Award No KUK-C1-013-04, made by King Abdullah University of Science and Technology(KAUST). AM's research is also supported by an EPSRC Career Acceleration Fellowship EP/J001686/1. The research leading to these results has received funding from the European Research Council under the *European Community*'s Seventh Framework Programme (*FP7/2007-2013*)/ ERC *grant agreement* No. 239870. RE would also like to thank Somerville College, University of Oxford, for a Fulford Junior Research Fellowship; Brasenose College, University of Oxford, for a Nicholas Kurti Junior Fellowship; and the Royal Society for a University Research Fellowship.

[1] E. Lueder, *Liquid crystal displays: Addressing schemes and electro-optical effects* (Wiley, 2010).
[2] B. Bahadur, *Liquid crystals: applications and uses*, vol. 1 (World Scientific Pub Co Inc, 1990).
[3] P. de Gennes and J. Prost, *The physics of liquid crystals* (Oxford University Press, USA, 1995), ISBN 0198517858.
[4] S. Kitson and A. Geisow, Applied physics letters **80**, 3635 (2002).
[5] A. Majumdar, C. Newton, J. Robbins, and M. Zyskin, Physical Review E **75**, 051703 (2007).
[6] T. Spencer, C. Care, R. Amos, and J. Jones, Physical Review E **82**, 021702 (2010).
[7] C. Tsakonas, A. Davidson, C. Brown, and N. Mottram, Applied physics letters **90**, 111913 (2007).
[8] A. Davidson and N. Mottram, Physical Review E **65**, 051710 (2002).
[9] F. Frank, Discussions of the Faraday Society **25**, 19 (1958).
[10] A. Majumdar, Submitted to Communications in Pure and Applied Analysis (????).
[11] R. Adams and J. Fournier, *Sobolev spaces*, vol. 65 (Academic press New York, 1975).
[12] A. Majumdar, J. Robbins, and M. Zyskin, Journal of Physics A: Mathematical and General **37**, L573 (2004).
[13] P. Krutitskii, Quarterly of Applied Mathematics **66**, 177 (2008).
[14] A. Majumdar and A. Zarnescu, Archive for rational mechanics and analysis **196**, 227 (2010).
[15] A. Majumdar, European Journal of Applied Mathematics **21**, 181 (2010).
[16] N. Mottram and C. Newton, University of Strathclyde, Department of Mathematics, Research Report **10** (2004).
[17] A. Rapini and M. Papoular, Le Journal de Physique Colloques **30**, 54 (1969), ISSN 0449-1947.
[18] F. Bethuel, H. Brezis, and F. Hélein, Calculus of Variations and Partial Differential Equations **1**, 123 (1993).

[19] R. Hardt, D. Kinderlehrer, and F. Lin, Communications in mathematical physics **105**, 547 (1986).
[20] L. Evans, *Partial Differential Equations* (American Mathematical Society, 1998).
[21] C. Johnson and C. Johnson, *Numerical solution of partial differential equations by the finite element method*, vol. 32 (Cambridge university press Cambridge, 1987).
[22] R. Seydel, *Practical bifurcation and stability analysis* (Springer Verlag, 2010), ISBN 144191739X.
[23] V. Streeter, E. Wylie, and K. Bedford, *Fluid mechanics* (McGraw-Hill, 1998).
[24] A. Iserles, *A first course in the numerical analysis of differential equations* (Cambridge Univ Pr, 2008), ISBN 0521734908.
[25] R. Wheeden and A. Zygmund, *Measure and integral* (Dekker, 1977).
[26] J. Hake, A. Logg, and G. Wells, *DOLFIN: A C++/Python finite element library*, Available from `https://launchpad.net/dolfin`.
[27] S. Strogatz, *Nonlinear dynamics and chaos: With applications to physics, biology, chemistry, and engineering* (Addison-Wesley Reading, MA, 1994).
[28] F. Gomes and D. Sorensen, *ARPACK++*, Available from `http://www.ime.unicamp.br/~chico/arpack++/`.